Chapter 5

Advanced Electron Microscopy Techniques in Nanomaterials Characterization at NASA Glenn Research Center

Francisco Solá

Additional information is available at the end of the chapter

http://dx.doi.org/10.5772/60532

Abstract

In this chapter, the author will review several advanced microscopy techniques developed at the NASA Glenn Research Center in the last 5 years. Topical areas include: unconventional approach to investigate the fine nanoporous structure of aerogels by scanning electron microscopy, new limits for transmission electron microscopy investigation of dispersion and chirality of single-walled carbon nanotubes within a polymer matrix, the importance of microstructure of porous tin dioxide nanostructure that lead to first time detection of methane at room temperature without doping or catalyst, in situ SEM methods to study the thermal stability of nanoparticles on Graphene/Cu based materials, electron beam irradiation effects on carbon nanotube yarns electrical properties, and nanoindentation work of multiphase thermoelectric material.

Keywords: Electron microscopy, Aerogels, CNT, SnO_2, Graphene/Cu, WSi_2/SiGe

1. Introduction

Nanomaterials can have a direct impact on NASA missions in areas of engineered materials and structures, devices, electronics, energy generation and storage, and sensors among others [1]. Nanomaterials can offer up to 50 percent weight savings, and thus cost [1]. This chapter will review several advanced microscopy techniques developed and applied to cutting-edge nanomaterials research at NASA Glenn Research Center (GRC) in the last 5 years [2]. The first

topic investigates the examination of the nanoporous structure of aerogels with a scanning electron microscopy (SEM) technique. Aerogels are emerging materials with the promise of unusually high strength (for some cases), thermal insulation, and damping capability combined with very light weight. Because of these properties, aerogels have been used in several NASA missions to collect comet dust particles and provide thermal insulation of components in Mars rovers, for instance [3]. Other current applications include thermal insulation for inflatable reentry decelerators and extra-vehicular activity suits [4]. Many of the outstanding physical properties of aerogels depend on their porous structure. SEM is a commonly used technique to estimate the pore size in aerogels, but is hampered by charging, the accumulation of electrons on the surface of the sample. The common solution employed to minimize charging effects is to deposit a layer of a conducting material on the sample. However, this technique can drastically mask the intrinsic porous structure of the aerogel. Here it is shown that negative charging effects on aerogels can be dissipated using nitrogen gas [5-6].

The second subject will be carbon nanotube (CNT)/polymer nanocomposites, which have excellent promise for improved strength and light weight and are being actively researched in a number of NASA projects. Recently this type of material has been used in the Juno mission for electromagnetic charge dissipation and electromagnetic shielding; other applications include lightning strike protection of aircraft [7-8]. Transmission electron microscopy (TEM) is a technique used to characterize the dispersion of nanotubes in a polymeric matrix. However, imaging such CNTs is challenging because of both their small size and electron scattering by the polymer matrix affecting the image contrast. This effort determined new limits for TEM investigation of dispersion and chirality of nanotubes in polymer matrices. This work opened new possibilities for investigation of microstructure of polymer nanocomposites to further understand electrical, mechanical, and thermal properties [9-10].

The third area is related to microstructure investigation and in-situ heating experiments on copper-based nanoparticles embedded in a graphene matrix. This material was considered by us for lithium ion battery applications. Lithium-ion batteries have been used at NASA in human and robotic spacecraft, because of their high power density and the weight savings compared with traditional nickel based batteries [11]. In a few years one lithium-ion battery will replace two nickel-hydrogen batteries in the International Space Station. Lithium ion batteries formed with nanostructured materials can potentially increase battery efficiency because of high surface-to-volume ratio, while reducing weight and cost. Here we were looking for oxygen content, dispersion of nanoparticles in the graphene, possibilities to anneal agglomeration of nanoparticels by heating, as well as perform extreme heating experiments. The heating experiments are sustained with theoretical treatments of both the thermal stability of the particles, as well as the most energetically favorable orientation relationships between the atomic planes of the particles and the graphene. Evidence of neck evolution, coalescence, sublimation, and Ostwald ripening were observed [12].

The fourth topic is on TEM characterization of the detail in new porous tin dioxide (SnO_2) nanorods as the sensing material for room-temperature methane detection [13-14], which has applications in environmental and engine emissions monitoring. Particular emphasis will be on establishing bonding type and particle size of SnO_2 within the porous structure, as these has been shown to influence the sensitivity of SnO_2 materials. We were able to establish the

http://dx.doi.org/10.5772/60532

rutile structure of tin dioxide by high-angle annular dark field (HAADF) imaging with atomic resolution as well as electron diffraction (ED). The tin dioxide chemistry was also confirmed by electron energy-loss spectroscopy (EELS) fine structure using two methods: (1) the position of the peaks in the 530–540 eV range, which are fingerprints for tin oxide structure, and (2) estimation of the ratio of Sn-Sn and Sn-O bond lengths distances, by the so-called resonance peaks at higher energies.

The fifth area is on electron beam irradiation effects on the electrical resistivity of CNT yarns. Yarns are currently been investigated for structural applications and potential replacement of conventional carbon fiber in composite materials, as well for wiring applications. One specific example is composite overwrapped pressure vessel (COPV) tanks. These types of tanks are used to contain high-pressure fluids in propulsion, science experiments, and life support applications [15]. COPVs offer a 50% weight savings compared with metal tanks. One critical aspect of the project was to improve the mechanical properties of this material. One potential route to achieve the mechanical improvement is the cross-linking method induced by electron beam irradiation. The study of the electrical response of CNT yarns as a function of electron dose is one route to monitor possible cross-linking events. In this work, small segments of CNT yarns were exposed to e-beam irradiation in a TEM. The electrical resistivity as a function of e-beam irradiation was studied by the two probe method, using micromanipulators inside a SEM [16-17].

Finally, nanoindentation and microstructure investigation of thermoelectric (TE) composites consisting of silicon germanium (SiGe) combined with tungsten silicides will be presented [18-19]. SiGe alloys have been traditionally used for radioisotope thermoelectric generators (RTGs) in several spacecraft and NASA missions such as Apollo [12, 14-17], Cassini, Galileo, and recently Curiosity [20]. We have been working on ways to improve the thermoelectric figure of merit (ZT) of SiGe based TE alloys by incorporating WSi_2 phases in to the matrix. It is predicted that the incorporation of nano-size WSi_2 into a SiGe matrix will yield the lowest thermal conductivity (and therefore represents the best case to maximize the ZT) when compared with other types of silicides. Beyond traditional RTG applications, we are exploring other uses in the energy-harvesting arena. These include multifunctional structures that generate power while reducing weight, sensor systems to monitor performance of engines, hypersonic vehicles, and others. Considerable effort has been focused on microstructural engineering methods that lead to ZT improvement by microstructural optimization of TE materials.

Although critical for the previous mentioned applications, work pertinent to the mechanical integrity of this type of WSi_2/SiGe based TE materials is limited. Nanoindentation is a suitable technique to probe the local hardness (H) and modulus (E) of a multiphase material at micron and submicron dimensions. Probing the mechanical properties of the phases of a bulk multiphase material is of fundamental importance as this in principle can dictate the overall mechanical properties of the bulk, as well as provide insight to improving its mechanical properties. In more practical scenarios, TE materials can be exposed to several perturbations during service, such as mechanical and thermal loading, mechanical vibrations, and thermal gradients that can lead to the formation of cracks, which can potentially degrade the transport

properties (by reducing the electrical conductivity). In this regard it is therefore critical to study the mechanical properties of TE materials. We will examine the local mechanical properties and microstructure of WSi_2/Si_xGe_{1-x} multiphase thermoelectric material by nanoindentation, electron, and focused ion beam microscopy (FIB) methods.

2. Aerogels

Aerogels are nanoporous materials with high pore volume, frequently greater than 90%. The tortuosity of the pore structure and thinness of the solid struts render the aerogels exceptional insulators by decreasing both gaseous and solid conduction [21-22]. It is critical to find ways to characterize the porous structure of aerogels, as this dictates the thermal properties. Both TEM and SEM techniques are commonly used to explore the pore size in aerogels [23-25]; however, both techniques suffer from charging effects. Precaution must be exercised during TEM investigation of these materials at the nanoscale, as local high electric fields resulting from charge accumulation can cause surface mass migration of SiO_x species and may form local areas with collapsed porous structures [26-28].

The most common solution to reduce charging effects of nonconducting materials (like aerogels) is to deposit a conducting material at the surface of the sample. Yet this approach usually masks, and can change the inherent porous structure of, the aerogel [25]. We have developed a new procedure to reduce charging effects of aerogels during SEM imaging. The process involves the local recombination of the negative charges caused by electron beam irradiation during imaging with positive ions created by ionization events induced from inert gas injection near the surface of the sample. High-energy backscattered electrons (BSEs) are created by multiple elastic scattering events and have relative high energies, whereas low-energy secondary electrons (SE) are produced by inelastic scattering events. The SE yield is denoted by δ, whereas BSE yield is symbolized with η. In general, a sample can be charged positively or negatively or be in a neutralized state during SEM investigation [12]. The law of charge conservation describes the process analytically. Generally,

$$I_{PE}\left[1-\left(\delta+\eta\right)\right]-I_L=\frac{\partial Q}{\partial t} \tag{1}$$

where I_{PE} is the current added to the sample by primary beam of electrons (PE), I_L is the outflow current and $\partial Q/\partial t$ is the charge build–up rate [29]. Therefore negative charging effects will be fulfilled when I_{PE} is greater than the total emission/leakage current. Penalties of this negative charging are the production of image distortion and unbalanced white contrast features.

Figure 1a is a SEM image of an aluminosilicate aerogel in which charging effects are noticeable. These artifacts and image distortions are caused by negative charging, where a negative potential deflects the PE imaging beam. For clarity, some distorted lines are marked with white solid arrows in figure 1a. It is well known that charging is usually not a static problem and

http://dx.doi.org/10.5772/60532

may change under scanning events [30]. The defocused lines can be described by a capacitor model that takes into consideration charging and discharging events. For more details see references [5, 31]. To reduce these charging effects we proposed a nonconventional approach. The key is to neutralize/minimized negative charging by the recombination with local ions. For the formation ions, dry nitrogen (N_2) gas is inserted near the surface of the sample. Details of the process can be found in reference 5. Collisions of electron signals with the nitrogen gas ionizes the N_2 molecules forming positive ions (N_2^+) according to $N_2 + e^- \rightarrow N_2^+ + 2e^-$, where the ionization energy is near 15.6 eV [32].

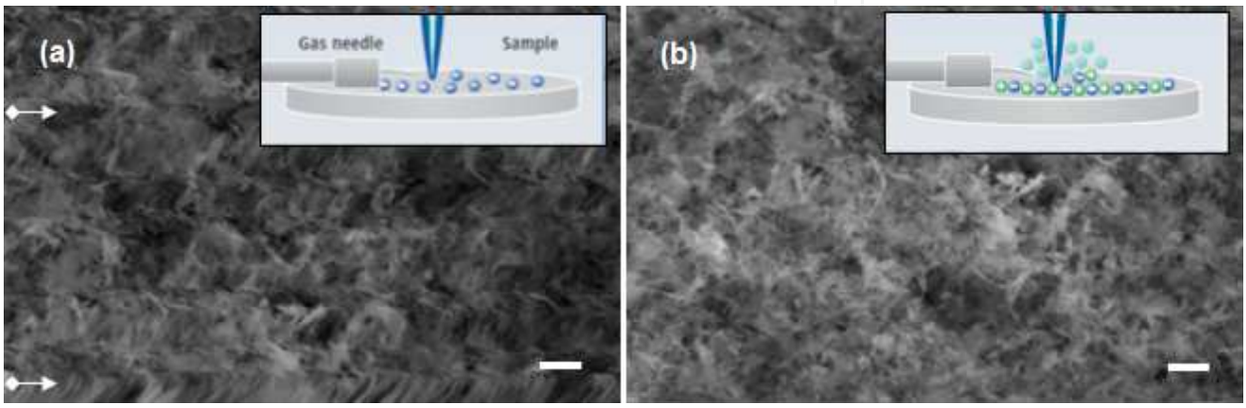

Figure 1. SEM images of aerogels with charging artifacts (gas needle off) (a) and when charge compensation device is working at 100% (b). Some artifact defocused lines are marked with solid arrows. Scale bar is 100 nm. Insets are the corresponding schematic representations of cases (a) and (b). Reproduced from reference 5 with permission from the Institute of Physics.

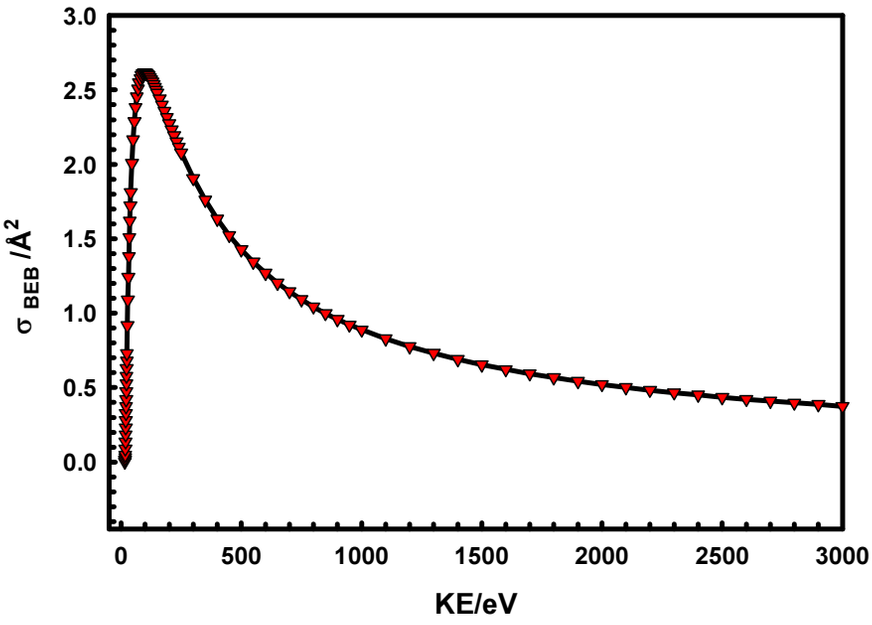

Figure 2. Predicted values for the N_2 ionization σ_{BEB} as a function of *KE* of electrons. Reproduced from reference 5 with permission from the Institute of Physics.

Consequently, N_2^+ ions are attracted to the sample surface by local electric fields, followed by recombination with negative charges and charge neutralization as pictured in the inset of figure 1b. Porous structure down to 3 nm where resolved. It is known that collisions with larger cross sections (σ) will produce more ions [33-34]. Figure 2 is the expected σ dependence of the kinetic energy (*KE*)for the electrons. The predicted values are based on the Binary-Encounter-Bethe (BEB) Model, which adds the Motts cross-section with the high *KE* factor and Bethe cross section [35]. The maximum value of σ_{BEB} (~ 2.62 Å^2) is produced with electrons with *KE* of ~100 eV, which corresponds to low energy BSE. For SE with energies of ~50 eV, σ_{BEB} is ~2.17 Å^2. However, if we consider the fact that most of the SE (~90%) have *KE* of 10 eV (or even less), which is below the ionization energy for N_2, ionization events by SE should be rare.

3. CNT/polymer nanocomposites

Numerous polymers have been used to synthesize CNT/polymer nanocomposites with the objective of achieving superior properties [36-40]. One key factor is the effective dispersion of fillers in the matrix. Still, dispersion is difficult as CNTs tends to agglomerate, causing weakening of the nanocomposite. The nature of the nanotube-polymer interface is particularly critical to the reinforcement of polymer matrices, where significant interfacial adhesion between the nanotube and surrounding polymer is essential. However, in the case of electrical properties and single-walled carbon nanotubes (SWCNTs), although the dispersion is important, the major control has to be focused in a reliable method to identify the abundance of metallic/semiconducting type of nanotubes through chirality [41]. Other important factors such as the CNTs alignment in the polymer matrix, as well as other common analyses involving distribution and quantification of nanotube dimensions can be explored by electron microscopy methods [10].

Although the resolution of a TEM can suffice to image SWCNTs, callenges do exist to image them in a polymer matrix and to explore its dispersion in an isolated form. Imaging individual SWCNTs in a polymer matrix is of great challenge because its small size and weak contrast signal typically is attenauted by the relatively strong polymer scattering signal. An example of this problem is shown in figure 3. It can be observed that while the SWCNT walls can be resolved in the hole (free standing) region, its contrast is lost in the polymer region.

New boundaries have been proposed to characterize SWCNTs within a polyethylene (PE)polymer matrix, by the assistance of modeling procedures [9]. A high-resolution TEM (HRTEM) image of a 25-Å nanocomposite of thickness (t) is presented in figure 4a. A HRTEM image of the same isolated SWCNT is included in the inset of figure 4a. Clearly the SWCNT walls can be resolved completely for the isolated case. However, even with a nanocomposite of t = 25 Å, a decrease in wall contrast signal as well as width is evident. In addition, the walls of the SWCNT totally vanish for a nanocomposite with t = 49 Å, as indicated in figure 4b. The interesting results are that ED analysis is less sensitive to these thickness problems. Figures 5a-c are ED patterns for isolated (5a), nanocomposite with thicknesses 25 Å (5b) and 49 Å (5c). Note that there are fingerprint reflection lines (D_i, i = 1, 2...4) in the isolated SWCNT that persist

http://dx.doi.org/10.5772/60532

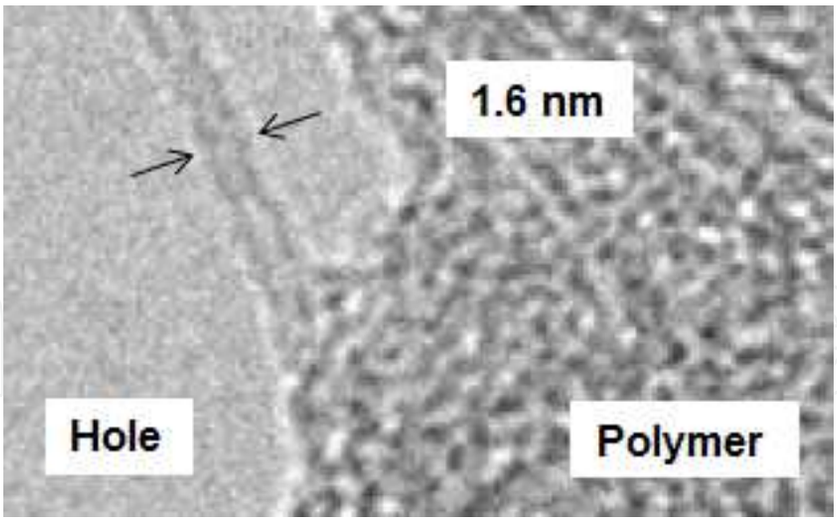

Figure 3. HRTEM of CNT in a polymer matrix. Reproduced from reference 10 with permission from Wiley/Scrivener.

for the nanocomposite cases in 5b and 5c. From these D_i distances both the diameter of the SWCNT and chirality can be estimated. This data can be used to understand the nanocomposite's electrical properties, by establishing the abundance of metallic and semiconducting nanotubes.

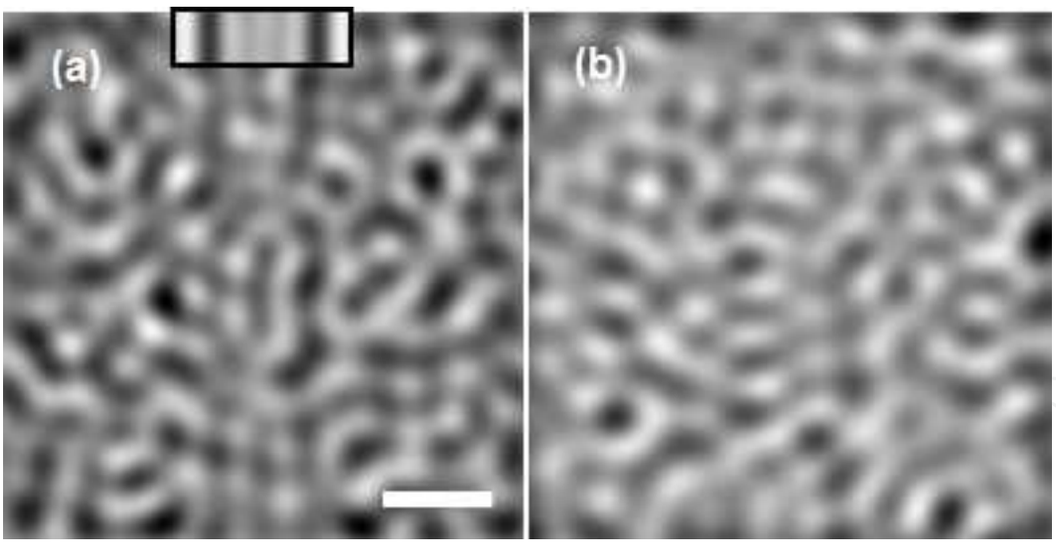

Figure 4. HRTEM simulations of SWCNT in PE matrix. Reproduced from reference 9 with permission from Wiley. Scale bar is 1 nm.

We also explored the case of nanotube walls oriented perpendicular to the electron beam and found that the nanotube can be resolved for a thicker nanocomposite, see reference 9. However, an apparent increase in nanotube diameter was evident event at optimum focus. As a result, estimating both chirality and diameter from HRTEM images will be erroneous in this case. Additionally, by combining results from data collected with the beam parallel and perpen-

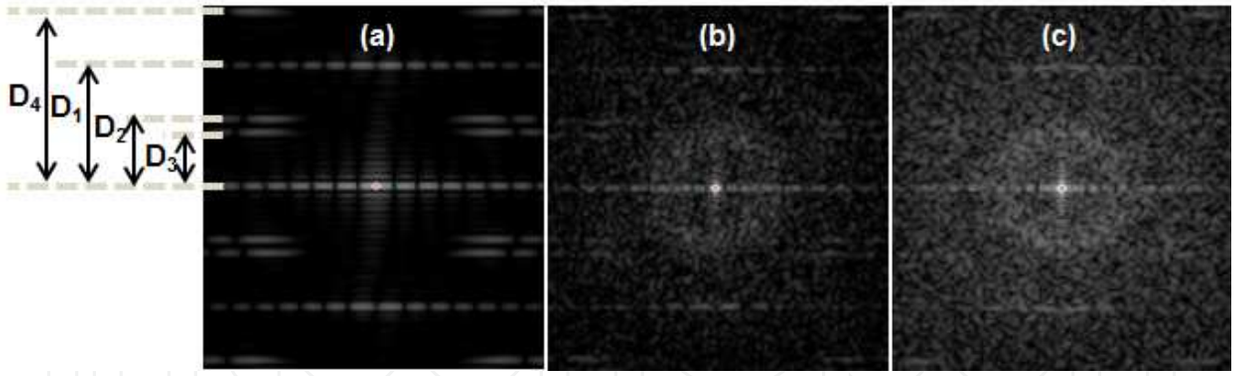

Figure 5. ED simulations of SWCNT in PE matrix. Reproduced from reference 9 with permission from Wiley.

dicular to the walls of the nanotube, it is possible to study dispersion of isolated SWCNT in a polymer matrix at the nanoscale level.

4. Graphene/Cu-based nanocomposites

Graphene materials have exceptional properties [44]. However, graphene/metal nanoparticle hybrids can have even superior properties than isolated or pure graphene material [45]. Applications in graphene/Cu-based hybrids include lithium ion batteries [46] and electronics [47, 48]. Electron microscopy, particularly in situ heating work, is a powerful technique to explore the stability of nanoparticle/graphene systems. In this section the stability of graphene/Cu-based hybrids is reported in a wide range of temperatures. Extensive microscopy analysis showed that the graphene material was decorated with Cu-based nanoparticles of different shapes and sizes. Identified nanoparticle shapes included: truncated nanocubes, octahedrons and its truncations, nanorods, triangular prisms, and decahedrons [49].

Figure 6 presents an energy-filtered TEM (EFTEM) EELS and selected area ED (SAED) analysis of the nanocomposite. Figure 6a is the zero-loss image, and figure 6b is the oxygen mapping [26]. We observed different degrees of oxidation, from partially oxidized (examples marked with dotted arrows) to fully oxidized nanoparticles. Likewise, some nanoparticles such as those marked with solid arrows in the figure were oxygen free. Based upon the results of figure 6 we were able to establish the presence of pure copper and copper oxide cubic phases [50]. Figures 7a to 7f present the low-magnification in situ SEM heating results where the whole composite could be observed. Evidence of coalescence (regions enclosed with solid circles), and Ostwald ripening (d regions enclosed with dotted circles) were observed [51-54]. The final individual nanoparticles transformed to spherical shapes in order to minimize the surface energy [55]. Numerical analysis of the neck formation between two nanoparticles was conducted to explore the initial steps of coalescence; the data is presented in figure 8. For two symmetrical spherical particles theory predicts that $D \sim t^b$, where t is time and $b \sim 0.143$ for surface diffusion or 0.167 for grain boundary diffusion [56]. The experimental value obtained for b was 0.518± 0.024. This higher value is in fact caused by faceting of the nanoparticles [57].

http://dx.doi.org/10.5772/60532

Molecular dynamics simulations were also conducted, taking into consideration facets of the nanoparticles that agreed with the experimental results [12]. In addition, MD results suggested that the growth rate of particle pairs on graphene was comparable to isolated pairs, which indicated that graphene had no significant effect on the coalescence. This effect may be consistent with a weak Cu-graphene interaction ("physisorption") as reported in other reports. We found that grain boundary energy was the main factor affecting the neck growth rate at the nanoscale. Sublimation experiments were also conducted, and it was observed that the {111} surfaces were more stable than {100}, which is consistent with predictions of Chatterjee's theory [58].

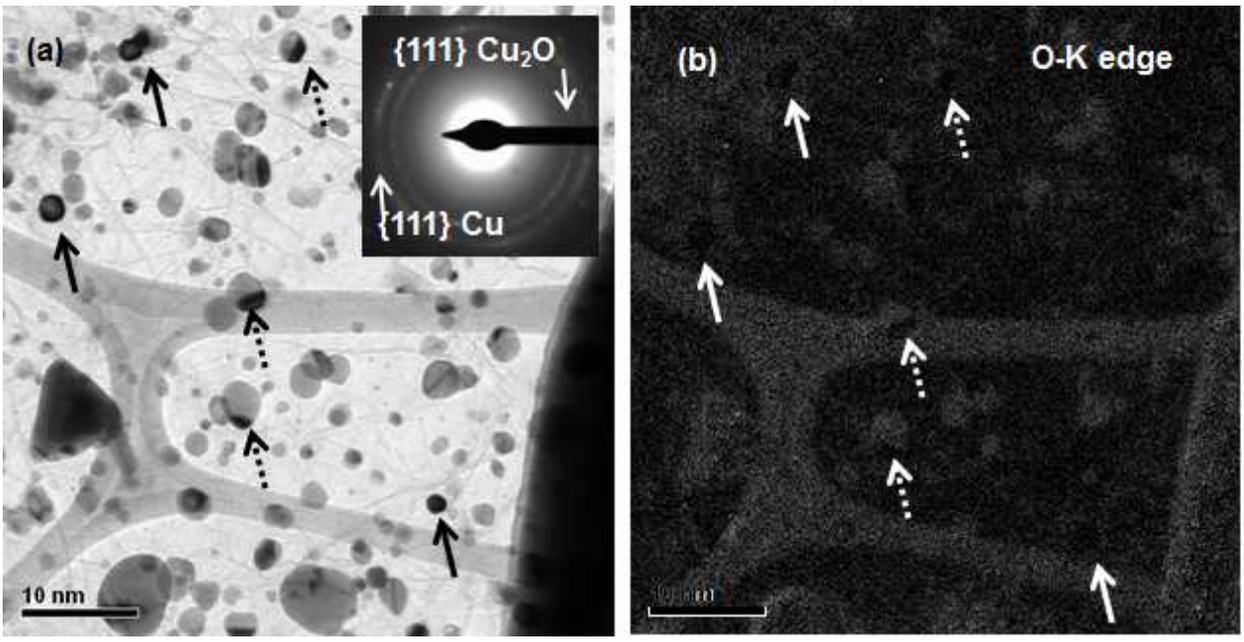

Figure 6. EFTEM and SAED analysis of the graphene/Cu-based nanocomposite. Reproduced from reference 12 with permission from the Institute of Physics.

5. Porous SnO_2 nanostructures

Semiconducting metal oxides like tin oxide (SnO_2) have been shown to respond to relevant chemical species such as oxygen (O_2), carbon monoxide (CO), ethanol (C_2H_5OH), nitric oxides (NO_x), propylene (C_3H_6), and hydrogen (H_2) [59-61]. Methane gas is highly volatile and when mixed with air can cause explosions at higher concentrations because it is readily flammable. Thus, the development of a reliable and cost-effective methane gas sensor is important. Room-temperature detection of methane is challenging and has been reported by others, but those lack the temperature range capability for realistic applications [62-69]. Recently NASA GRC developed porous SnO2 nanostructures for methane detection for a wide temperature range, including room temperature [13].

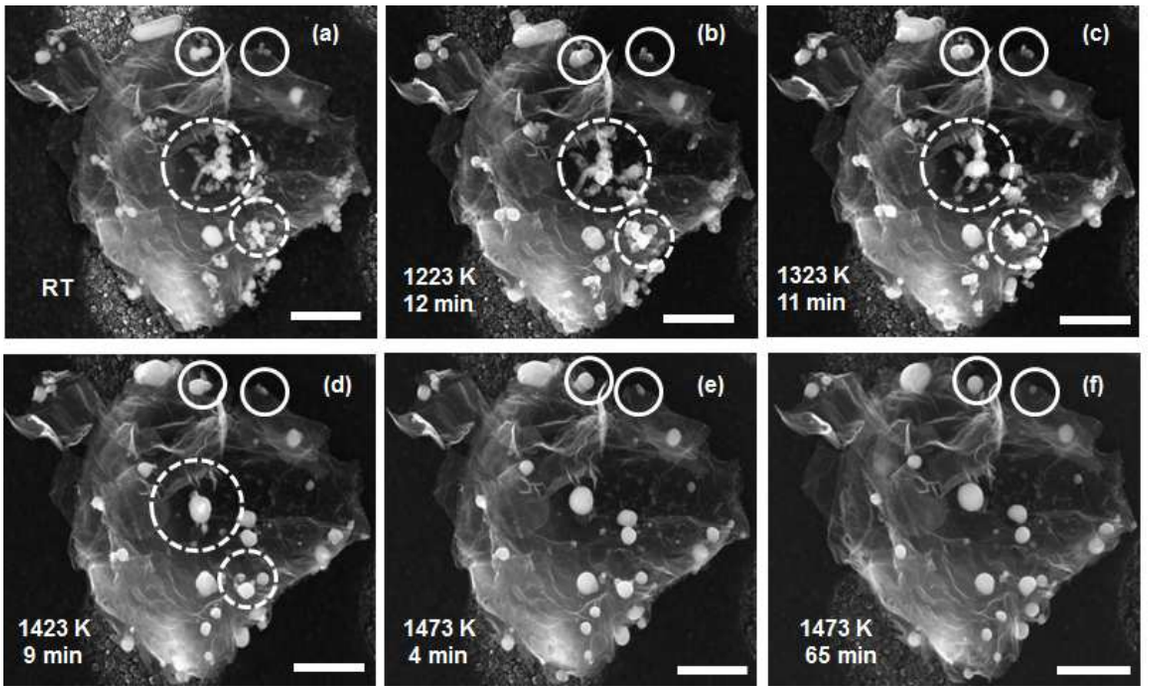

Figure 7. SEM images of microstructural evolution of a graphene sheet decorated with Cu nanoparticles in full view, as a function of temperature and time (a)–(f). Reproduced from reference 12 with permission from the Institute of Physics. Scale bar is 1μm.

The sensor was operated at room temperature and detection of 0.25% methane in air was demonstrated for the first time, without the use of any dopants or catalysts. Porous SnO_2 nanorods were synthesized using MWCNTs as templates, as indicated in figure 9. The process involves the decoration of MWCNTs with SnO2 nanoparticles (fig. 9a), followed by calcination of nanotubes at higher temperatures in air, the end product being a porous structures as pictured in figure 9b. The inset of figure 9b is the corresponding SAED pattern of the porous SnO_2 nanorods. Figure 9c is a HRTEM image of the nanocrystals in the porous SnO_2 nanorod. Both analyses indicated the rutile SnO_2 structure [13, 60].

Furthermore, EELS analysis confirmed the SnO_2 structure by two methods (see fig. 10): (1) determining the fingerprint of this rutile structure by the presence of unique peaks in the 530–540 eV energy range [70] and (2) estimating bond length (r), by the use of $\Delta E = k/r^2$, where k is a constant [71]. For example, for the peak at 543 eV, $\Delta E_1 = 10.9$ eV, and for the peak at 558.5 eV, $\Delta E_2 = 26.4$ eV. It follows that $r_1/r_2 = 1.556$, which agrees well with the ratio of bond length values of SnO_2 nanograins, for the second Sn-Sn (= 3.19 Å) and first Sn-O (= 2.05 Å) coordination shells [72]. The rutile structure of tin di-oxide was also resolved by HAADF imaging with atomic resolution as indicated in the inset image of figure 10.

6. CNT Yarns

NASA is exploring routes to replace conventional carbon fiber composites with CNT-based composite materials. This could traduce in approximately one-third reduction of unfueled

http://dx.doi.org/10.5772/60532

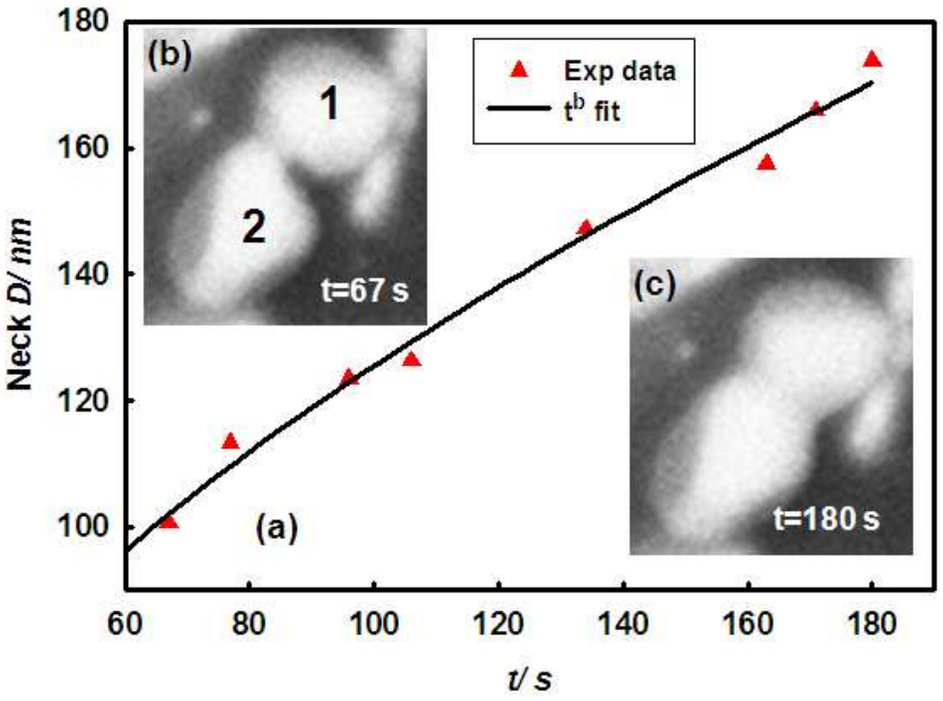

Figure 8. Quantitative neck evolution of two nanoparticles at 873 K shown graphically and with snapshots from a movie. Nanoparticle 1 had a diameter of ~ 250 nm, and nanoparticle 2 had a diameter of ~265 nm. (a) Plot of neck diameter, (b) and (c) are snapshots at 67 s and 180 s, respectively. Reproduced from reference 12 with permission from the Institute of Physics.

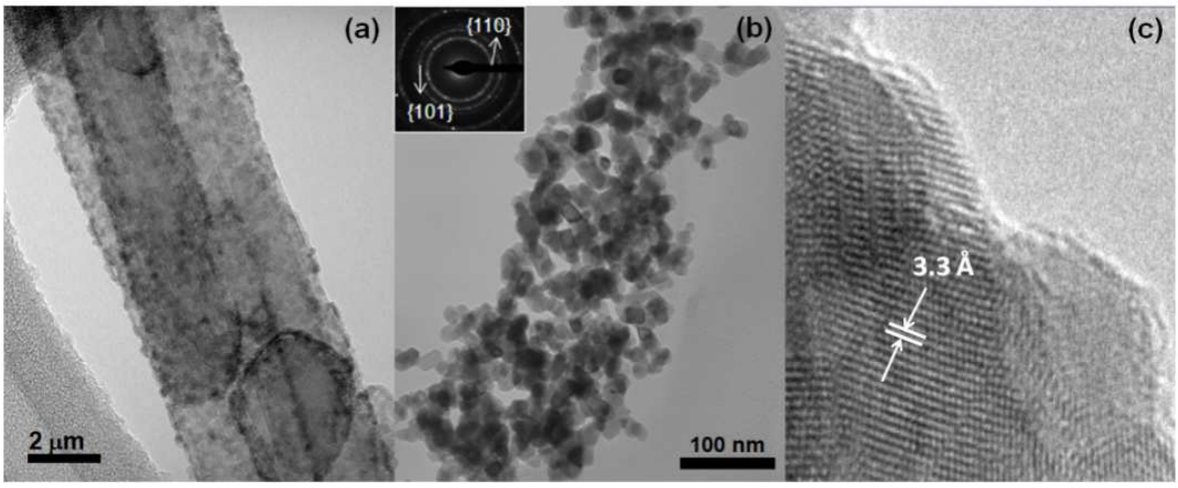

Figure 9. (a) TEM image of MWCNT covered with SnO_2 nanoparticles. (b) TEM image of a porous SnO_2 nanorod. Inset shows the ED pattern. (c) HRTEM image showing that the lattice spacing corresponds to the rutile structure of SnO_2. Reproduced from reference 13 with permission from the Institute of Physics.

weight of space vehicles and structures. To achieve this, commercially available CNT-based materials must have at least two times the strength of conventional carbon fibers. CNT yarns are currently the best commercially available CNT-based materials in terms of mechanical properties; however, their tensile strength is about half of conventional carbon fibers. This has

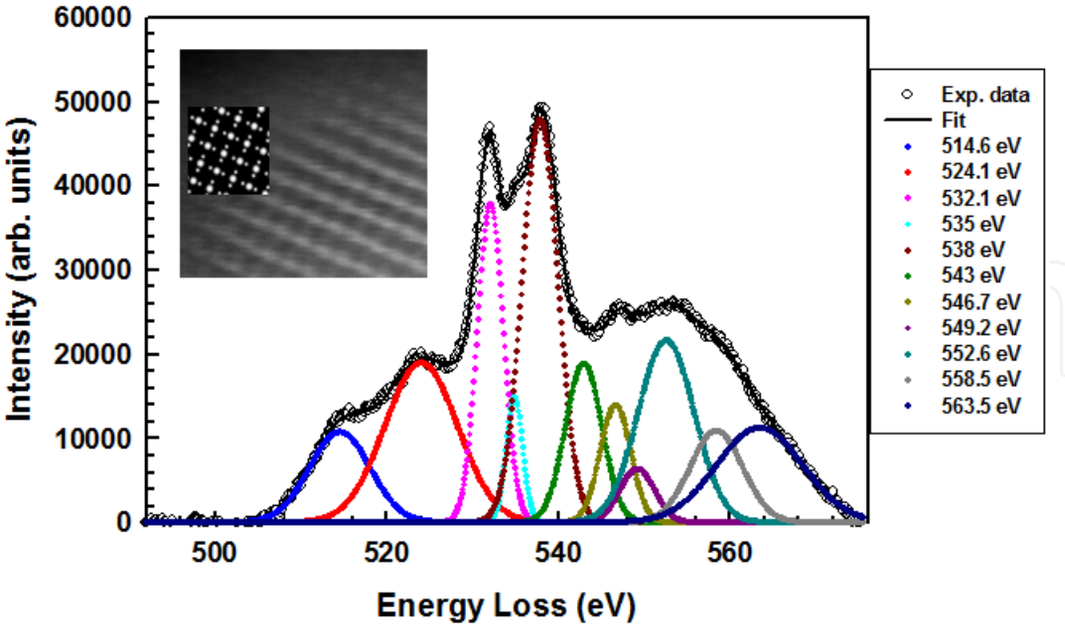

Figure 10. EELS spectrum of porous SnO_2 nanorods with its corresponding fit. Reproduced from reference 13 with permission from the Institute of Physics. The inset is atomic-resolution HAADF image.

to be with the weak shear interactions between carbon shells and bundles within a yarn [73-74]. Therefore, current efforts focus on developing protocols to improve mechanical properties of these materials.

One potential route to achieve mechanical improvement is the cross-linking method induced by electron beam irradiation. The weak shear interactions between adjacent carbon shells/CNT can be improved by the formation of sp^3 C-C bonds induced by e-beam irradiation [73]. This can occur at both the interwall sites of individual multiwall CNTs (MWCNTs) and between CNT neighbors, and both potentially will increase the mechanical response of CNT yarns [73, 76]. E-beam energies greater than 80 keV are needed to displace C atoms and to induce complex kinetics and recombination of lattice defects within the hexagonal carbon network, which eventually leads to cross-linking [77]. For one isolated MWCNT (and small bundles), energies at 100–200 keV are effective to cross-link [77]. Because CNT yarns are fibers composed of several MWCNTs, the question arises as to what extent energies in this range will still promote crosslinking effectively.

The study of the electrical response of CNT yarns as a function of electron dose can be a complementary route to monitor possible cross-linking events, and is important to establishing multifunctional properties of CNT yarns. Considerable effort has been focused in e-beam irradiation methods that lead to mechanical improvement. Although Mikó and coworkers reported the effects of e-beam irradiation on electrical resistivity of single-walled CNT (SWCNT) fibers systems [78-79], work on e-beam irradiation effects on electrical properties of CNT yarns is limited. Here, small segments of CNT yarns are exposed to e-beam irradiation in a TEM operated at 200 keV and different doses. The electrical resistivity as a function of e-beam irradiation is studied by the two-probe method, using micromanipulators inside a SEM.

http://dx.doi.org/10.5772/60532

The inset of figure 11 is a SEM image that illustrates the two-probe electrical characterization of CNT yarns. Typically the measurements were conducted to probe CNT yarns of ~450 μm in length and ~77–84 μm in diameter. The electrical resistivity as a function of e-beam irradiation is presented in figure 11. Irradiation times range from 10 to 60 min, which corresponds to dosages of ~$3x10^{15}$–$2x10^{16}$ e/cm^2. The average values of resistivity increased with irradiation time up to 30 min and decreased with further irradiation. Note that the maximum resistivity at 30 min of irradiation corresponds to an increase of ~1.5 times the resistivity of the pristine yarn, and that the resistivity at 60 min is just a slight decrease of the pristine resistivity. For comparison purposes, the resistivities of CNT yarns in the current study are about 10^2 times smaller than aerosol-like (nontwisted) yarns, but are ~10^3 times higher than other twisted yarns, though these values were estimated with a yarn segment length of 50 mm [80], and about 10 times higher than SWCNT fibers of 3–5 mm tested length [78, 79].

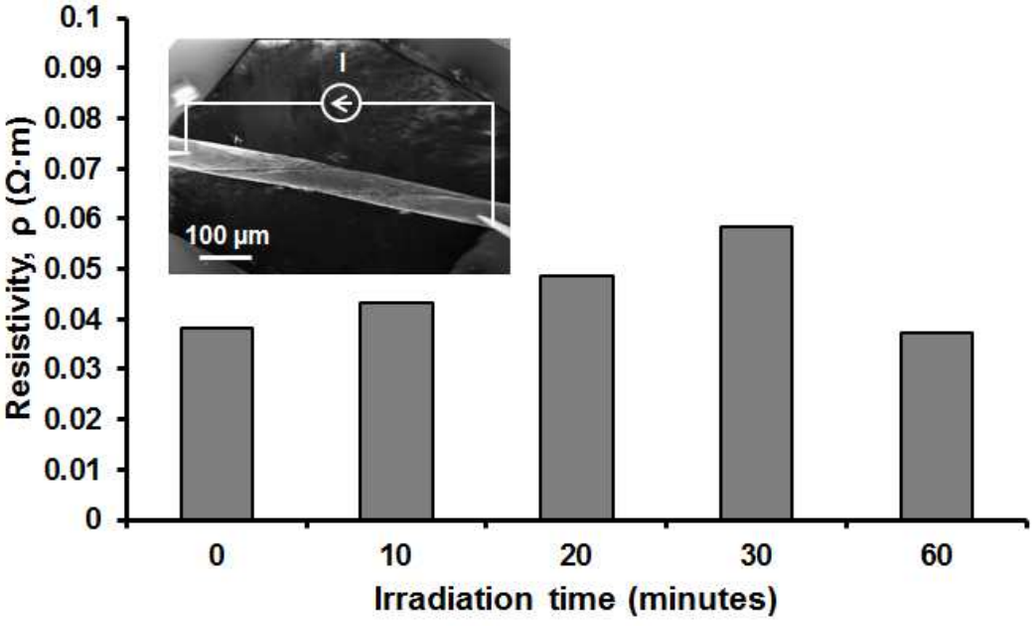

Figure 11. Effect of e-beam irradiation on CNT yarn resistivity. The inset is an SEM image of two tungsten probe electrical setup measurement. Reproduced from reference 16 with permission from OMICS Publishing Group.

To obtain possible explanations to the e-beam irradiation effects on resistivity, HRTEM analysis on the microstructure of CNT yarns were conducted. Figure 12 presents the HRTEM of CNT yarns of pristine (12a), e-beam irradiated with10 min (12b), 20 min (12c), 30 min (12d), and 60 min (12e). Figure 12f is a schematic that summarizes possible crosslinking sites (marked with red lines) of CNT constituents within the yarn at two different scales. The images were taken in thin areas located at the edges of the yarns so one can see the different planes of CNTs oriented in a given twisted direction. For the purpose of the following discussion, only areas of the images that are in focus are described. The area enclosed by a white circle in figure 12a shows that the CNTs of yarns are double walled, and the area enclosed by a black circle is consistent with a CNT bundle structure. The alternating black/white fringes correspond to the lattice planes of CNTs in the bundle, with each lattice plane built from a row of CNTs [81].

Crosslinking sites in CNTs can be monitored by these HRTEM images and typically correspond to areas were the fringes are less coherent but do not completely lose their structure to form an amorphous carbon (a-C) structure [75]. Cross-linking events can be observed at 10 min of irradiation (fig. 12b). Several types of microstructural changes of CNTs within the yarn are evident at 20 min of irradiation (fig. 12c). These includes cross-linked sites (area enclosed by a black box), pristine-non-cross-linked sites (yellow box), a-C structure sites (red box) [82-87], and sites with a mixture of a-C and cross-linked sites (white box). With further irradiation it can be noticed that both a-C and cross-linked sites grows; however, overall the crystallinity (fringes structure) of CNTs is preserved (in the sense that it is not totally lost).

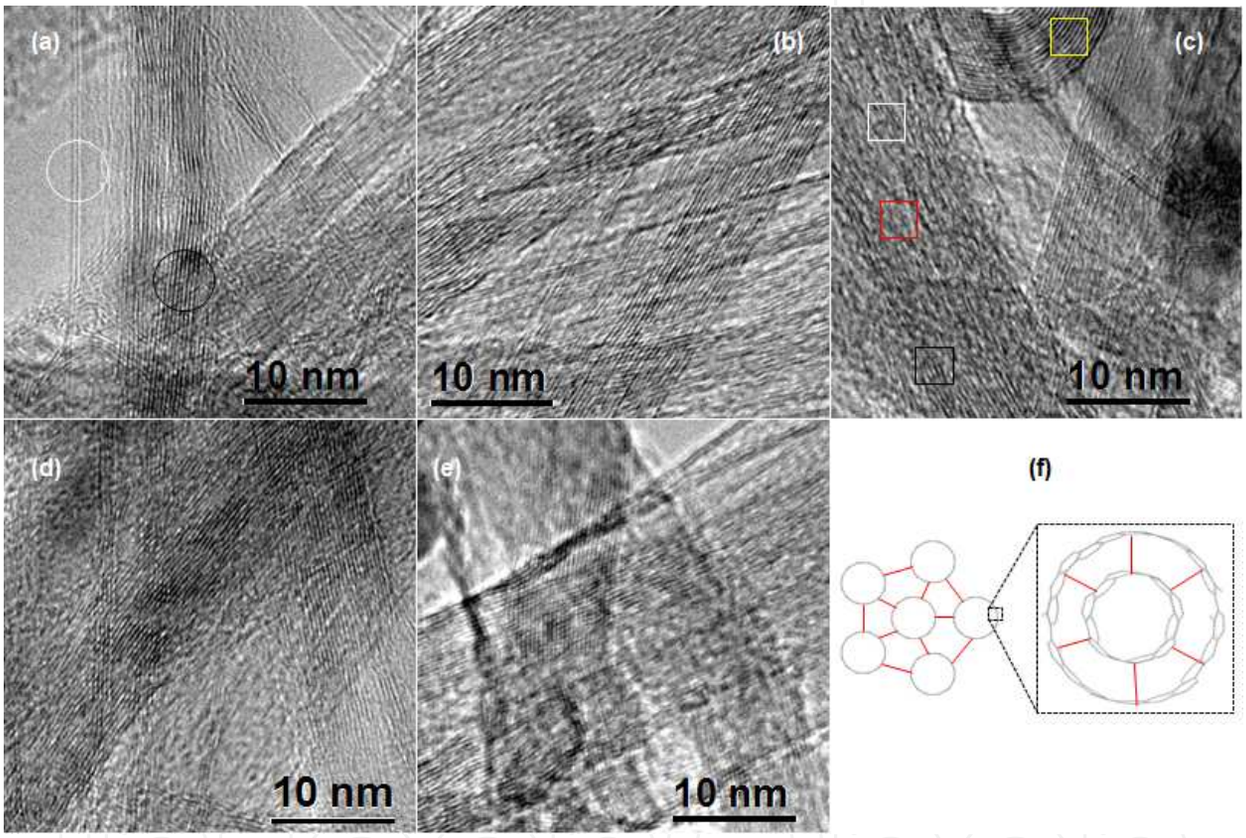

Figure 12. HRTEM of CNT yarns of pristine (a) and e-beam irradiated for10 min (b), 20 min (c), 30 min (d), and 60 min (e). (f) Schematic that explains possible crosslinking sites of CNT within the yarn, which are at bundle and isolated nanotube sites. Reproduced from reference 16 with permission from OMICS Publishing Group.

In order to understand these microstructural changes and how to correlate them with the corresponding resistivity results, a brief explanation on e-beam irradiation on CNT defect formation is needed. E-beam electrons can displace C atoms located at the hexagonal lattice network of CNTs only when critical minimum energy is used, known as the displacement threshold. However displacement threshold depends on the local arrangement of carbon atoms relative to the electron beam and type of CNT. This has to be with the direction of momentum transfer to C atoms distributed in the hexagonal lattice. For instance, displacement threshold energies of 82 keV have been reported for small CNTs oriented perpendicular to the

http://dx.doi.org/10.5772/60532

e-beam, and up to 240 keV for relative bulky CNTs oriented tangential to the e-beam [77]. For MWCNTs, displacement threshold energies correspond to 100 keV [77]. Once C atoms are displaced, lattice defect formation in the form of interstitials and vacancies will take place. Based on quantum mechanics calculations, defects on the form of divacancies, interstitials, and Frenkel pair (interstitial-vacancy pair) defects were shown to crosslink graphitic layers [88]. However, at the same time e-beam irradiation can lead to unwanted loss of lattice coherence, a processes known as amorphization. This has to be with the kinetics of defects (production rate, dynamics) on specific sites of the C lattice, and agglomeration of point defects that leads to larger defects. Dynamics of defects depends on temperature. E-beam irradiation at room temperature (as in this work) leads to the formation of vacancies and interstitials (for energies above the threshold energy), which remain relatively localized (immobile) at specific lattice sites. If they do not recombine to form cross-linking sites, high concentration and agglomeration of defects can occur as e-beam time increases, which eventually cause the lattice to lose its crystallinity at those sites. This model is consistent with the amorphous regions encountered in figure 12c–12e.

In terms of electrical results, the data can be explained in terms of a competitive process between cross-linking and amorphization. Cross-linking sites reduce the resistivity by reducing the CNT-to-CNT distance, while amorphization increases resistivity. Note that the reduction of resistivity by cross-linking events is not due to conduction of electrons through sp^3 C-C bonds. The increase in resistivity with10 min of e-beam irradiation can be explained by the formation of defects in the lattice that have not produced enough cross-linking sites to enhance conductivity. At irradiation times of 20–30 min, although cross-linking events are increasing, the resistivity is dominated by amorphization events. The reduction of resistivity at 60 min can only be explained by a significant increase in cross-linking population dominating the overall electrical conduction of electrons in the yarn. This is consistent with the microstructural data presented in figure 12.

7. WSi_2/SiGe composites

Figure 13a is a SEM image of the sample showing the typical sample microstructure of a WSi_2/SiGe composite. Note that there are micron-size as well as submicron-size grains within the microstructure. Standardless EDS point analysis in atomic percentage (at%) of region 1 marked with a black arrow indicated content of ~ 77 and ~23 at% for Si and Ge, respectively, whereas for region 2 ~91 at% (Si) and ~9 at% (Ge) were obtained. For simplicity regions of type 1 will be defined as Ge rich regions, and regions of type 2 will be referred to as Si rich. The local variations in Si and Ge content are caused by segregation during non-equilibrium solidification. These two regions contain grains of about 1–10 μm in size. Furthermore, the W:Si at% ratio of the region marked with the white arrow was ~1:2 consistent with a WSi_2 phase. We refer to the WSi_2 phase as those grains in the ~1–13 μm size range. The rest will be referred to as the matrix. The matrix actually comprises nanosized WSi_2 with grains down to ~3 nm, SiGe of uniform composition with sizes in the micron size range (upper value of ~15 um) and nanometer size range (lower value of ~120 nm), and some porosity.

Figure 13 presents SEM images showing examples of nanoindentation impressions (NI) for WSi_2 phase (13b), matrix (13c), WSi_2/matrix interface (13d), and Ge rich phase (13e). An example of WSi_2/matrix interface impression is included to show the level of positioning resolution of the diamond tip; however, no mechanical data related to interfaces will be included in this work. Figure 13f is an example of a SEM/FIB image cross section of a crack below the surface of a Ge-rich phase. Loads of 0.0012 N were used in NI on figures 13a–c, while 0.01 N was used in figures 13d and e. Note that the SEM image of figure 13f was taken with the sample oriented at an angle of 54 degrees relative to the electron beam and normal to the ion beam for the milling process. The inset of figure 13f is the surface view of the NI SEM image (also taken at 54 degrees), where the radial cracks can be noticed. As a final step, a protective material is deposited at the top of the NI area followed by the formation of two laterals and one front trench for cross section serial sectioning, as indicated in figure 13f.

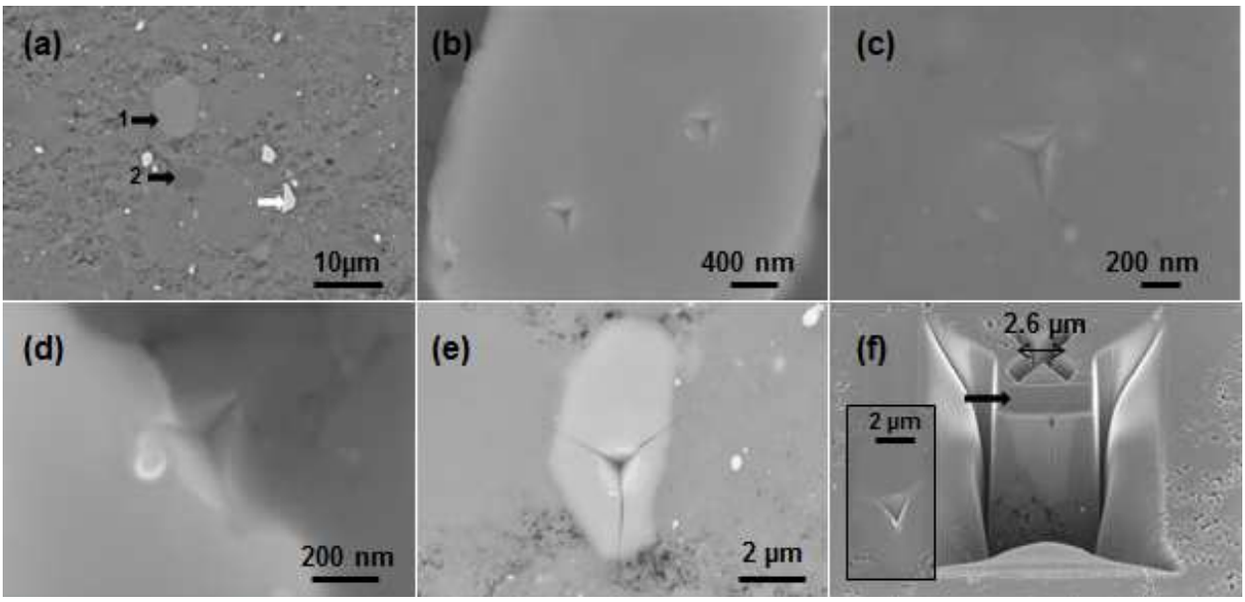

Figure 13. (a) SEM image showing the microstructure of the TE sample. SEM images showing examples of nanoindentation impressions for the WSi_2 phase (b), matrix (c), WSi_2/matrix interface (d), and Ge rich phase (e). (f) SEM/FIB image cross section of a crack below the surface of a Ge rich phase. Reproduced from reference 18 with permission from Elsevier.

Quantitative results for H and E for all phases can be found in figure 14a. For this analysis, a load of 0.0012 N was used. Average H (and E) values (in GPa) of 12.94 (464.95) for the WSi_2 phase, 19.49 (214.52) for the matrix, 14.95 (142.84) for the Si-rich phase, and 13.98 (138.56) for the Ge-rich phase. Figure 14b gives k_c for different phases, formed with data taken at a 0.02-N load for the WSi_2 and 0.01-N load for other phases, and average values of H and E. Fracture toughness was estimated using the relation $k_c = \alpha(E/H)^{0.5}P/c^{1.5}$, where P is the load, c is the total length of the radial crack, and $\alpha = 0.032$ for a cube-corner diamond tip [19]. Note that in order to estimate k_c, $c/a \geq 2.5$ must be true [24], where a is the diagonal length of the impression area. Average k_c values (in MPa•$m^{0.5}$) were 1.37 for the WSi_2, 0.52 for the matrix, 0.36 for the Si rich phase, and 0.24 for the Ge-rich phase. Furthermore, cross-sectional TEM analyses of the

http://dx.doi.org/10.5772/60532

deformation zone showed evidence of crack formation, dislocations, shear fault formation, and crack-induced amorphization; while serial sectioning FIB/SEM showed evidence of median and lateral cracks. The complete set of data is reported elsewhere [18]. SEM images illustrating the lift-out method for TEM analysis for the WSi_2 phase are presented in figure 15. Again, note that the SEM images are oriented at an angle of 54 degrees relative to the electron beam and normal to the ion beam (see fig. 15 a-b). Figure 15c presents a low-magnification bright-field (BF) TEM image of the deformation zone enclosed by a black box. The corresponding dark-field (DF) TEM image of the region enclosed in figure 15c is presented in figure 15d, which shows a crack (white arrow), high density of dislocations around the nanoindentation area (as well as the by the area enclosed with the white circle), and shear faults lines (solid white arrows); the inset is a schematic of shear lines. A dotted white arrow points to a crack.

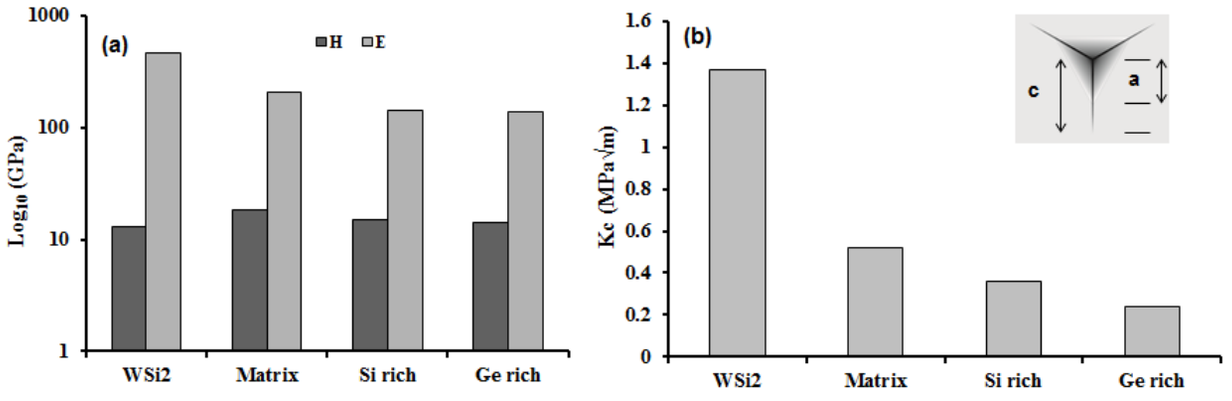

Figure 14. (a) Quantitative results for H and E for all phases. (b) k_c values for all phases. The inset is a schematic of radial crack formation induced by nanoindentation. Reproduced from reference 18 with permission from Elsevier.

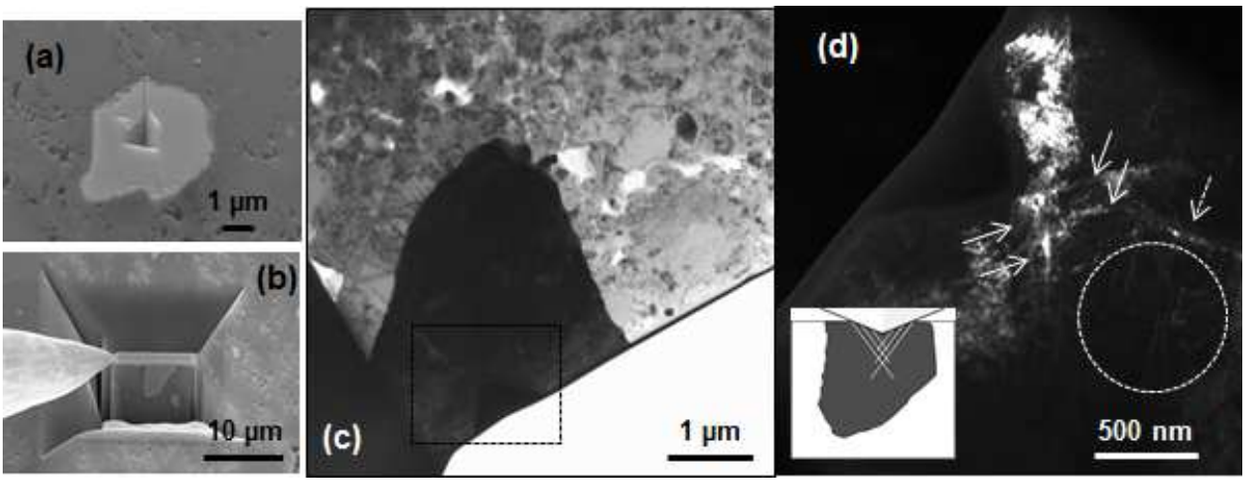

Figure 15. (a)-(b) SEM images illustrating the lift-out method for TEM analysis for the WSi_2 phase. BF-TEM (c) and DF-TEM (d) images showing the deformation zone. Reproduced from reference 18 with permission from Elsevier.

Based on the data obtained in this work, particularly on the superior hardness values and decent fracture toughness of the matrix (~45% upper value relative to pure WSi_2 phase) we proposed the following to obtain a robust TE WSi_2/SiGe material: (1) the segregation problem must be corrected, and (2) the porosity content needs to be minimized, as this will improve the mechanical properties as well as the electrical conductivity (and hence ZT). Higher population of nanosizes and less (or no) micron sized WSi_2 grains are needed. A higher population of nanosized WSi_2 will not only improve mechanical robustness, but can also improve ZT as well. Predictions by Mingo et al. [91] showed that WSi_2 nanoparticles below 30 nm in SiGe alloys will increase ZT considerably, with the optimum results being in the 2–10 nm range.

Acknowledgements

The author would like to acknowledge the collaborators who provided professional contributions to several topics covered in this book chapter. These include internal collaborators A. Biaggi-Labiosa (Sensor), F. Dynys (TE), F. Hurwitz (Aerogels), M. Meador (CNT/polymer), M. Lebrón (CNT/polymer); and external collaborators Z.H. Xia and J. Niu (CNT/polymer, Cu/G: U. North Texas), J. Yang (Aerogels: Carl Zeiss Microscopy). Technical support from J. Buehler, R. Rogers and M. Yoonessi is also acknowledged. This work was supported by the following projects: Hypersonic, Subsonic Fixed Wing, Vehicle Systems Safety Technologies, CNT Materials Development, and Advanced TE.

Author details

Francisco Solá

Address all correspondence to: francisco.sola-lopez@nasa.gov

Materials and Structures Division, NASA Glenn Research Center, Cleveland, OH, USA

References

[1] Meador MA, Files B, Li J, Manohara H, Powell D, Siochi EJ. NASA: Nanotechnology roadmap. http://www.nasa.gov/pdf/501325main_TA10-Nanotech-DRAFT-Nov2010-A.pdf (accessed 12 January 2015).

[2] Solá F. Latest developments in advanced electron microscopy techniques on nanomaterials at NASA Glenn Research Center. NTRS 2014; http://ntrs.nasa.gov/search.jsp?R=20140013326 (accessed 13 January 2015).

[3] National Aeronautics and Space Administration. NASA: STARDUST mission. http://stardust.jpl.nasa.gov/tech/aerogel.html (accessed 12 January 2015).

[4] National Aeronautics and Space Administration. NASA: Aerogels thinner, lighter, stronger. http://www.nasa.gov/topics/technology/features/aerogels.html (accessed 12 January 2015).

[5] Solá F, Hurwitz F, Yang J. New scanning electron microscopy approach to image aerogels at the nanoscale. Nanotechnology 2011; 22: 175704.

[6] Solá F, Hurwitz F, Yang J. New approach to image aerogels by scanning electron microscopy. APS March Meeting Abstracts 2011; 1: 1203.

[7] National Aeronautics and Space Administration. NASA: Mission Juno http://missionjuno.swri.edu/ (accessed 12 January 2015).

[8] Lebrón-Colón M, Meador M, Gaier JR, Solá F, Scheiman DA, McCorkle LS. Reinforced thermoplastic polyimide with dispersed functionalized single wall carbon nanotubes. ACS Applied Materials and Interfaces 2010; 2: 669.

[9] Solá F, Xia Z, Lebrón-Colón M, Meador MA. Transmission electron microscopy of single wall carbon nanotube/polymer nanocomposites: A first-principles study. Phys Status Solidi RRL 2012; 6: 349-351.

[10] Solá F. SEM and TEM characterization of polymer CNT nanocomposites. In: Mittal V (ed.) Polymer Nanotube Nanocomposite: Synthesis, Properties, and Applications. Wiley/Scrivener; 2014. p167-185.

[11] National Aeronautics and Space Administration. NASA: The heartbeat of the mars exploration rovers.https://solarsystem.nasa.gov/scitech/display.cfm?ST_ID=252 (accessed 13 January 2015).

[12] Solá F, Niu J, Xia Z. Heating induced microstructural changes in graphene/Cu nanocomposites. J Phys D: Appl Phys 2013; 46: 065309.

[13] Biaggi-Labiosa AM, Solá F, Lebrón-Colón M, Evans LJ, Xu, JC, Hunter GW, Berger G, González JM. A novel methane sensor based on porous SnO_2 nanorods: room temperature to high temperature detection. Nanotechnology 2012; 23: 455501.

[14] Biaggi-Labiosa A, Evans LJ, Xu JC, Hunter GW, Berger G, Solá F. Gas sensing properties of hybrid SnO2/carbon nanotubes. APS Meeting Abstracts 2011; 1, 21013.

[15] McLaughlan PB, Forth SC, Grimes-Ledesma LR. Composite overwrapped pressure vessels, a primer. NASA/SP 2011; 573: 1-20.

[16] Solá F. Electrical properties of pristine and electron irradiated CNT yarns at small length scales. Mod. Chem. and Appl. 2014; 2: 116.

[17] Solá F. Electrical properties of pristine and electron irradiated CNT yarns at small length scales: an electron microscopy study. Microscopy and Microanalysis 2013; 19 (S2): 518.

[18] Solá F, Dynys F. Probing the mechanical properties and microstructure of WSi_2/Si_xGe_{1-x} multiphase thermoelectric material by nanoindentation, electron and focused ion beam microscopy methods. J. Alloys Comp. 2015; 633: 165.

[19] Solá F, Dynys F. Probing the mechanical properties and microstructure of WSi_2/Si_xGe_{1-x} multiphase thermoelectric material by nanoindentation, electron and focused ion beam microscopy methods. Bulletin of the American Physical Society 60, 2015. http://absimage.aps.org/image/MAR15/MWS_MAR15-2014-000590.pdf (accessed 14 January 2015).

[20] Abelson RD. Space missions and applications. In: Rowe DM (ed.) Thermoelectrics handbook macro to nano. CRC press, Taylor & Francis Group; 2006. p874.

[21] Aegerter MA, Leventis N, Koebel MM. Aerogels handbook. Springer publishing; 2011. ISBN 978-1-4419-7477-8.

[22] Fricke J, Emmerling A. Aerogels. Adv. Mater. 1991; 3: 504.

[23] Stroud RM, Long JW, Pietron JJ, Rolison DR. A practical guide to transmission electron microscopy of aerogels. J. Non-Cryst. Solids 2004; 350: 277.

[24] Vacher R, Courtens E, Stoll E, Böffgen M, Rothuizen H. Pores in fractal aerogels and their incidence on scaling. J. Phys. Condens. Matter 1991; 3: 6531.

[25] Pajonk GM, Venkateswara-Rao A, Parvathy NN, Elaloui E. Microstructural characterization of silica aerogels using scanning electron microscopy. J. Mater. Sci. 1996; 31: 5683.

[26] Solá F, Resto O, Biaggi-Labiosa A, Fonseca LF. Electron beam induced growth of silica nanorods and heterostructures in porous silicon. Nanotechnology 2007; 18: 405308.

[27] Solá F, Resto O, Biaggi-Labiosa A, Fonseca LF. Electron-beam induced growth of silica nanowires and silica/carbon heterostructures. MRS Proceedings 2007; 1017: 1017-DD12-31.

[28] Betancourt J, Zypman F, Solá F, Resto O, Fonseca LF. The influence of roughness on the mechanical spectroscopy of SiO_2 nanorods grown by e-beam irradiation. Superlattices and Microstructures 2009; 45: 458-468.

[29] Cazaux J. Charging in scanning electron microscopy "from inside and outside". Scanning 2004; 26: 181.

[30] Reimer L. Scanning electron microscopy: physics of image formation and microanalysis, Springer series in optical sciences, 45, Ed: P.W. Hawkes (Springer-Verlag, Berlin, Germany), Ch. 3. ; 1998.

[31] Goldstein J, Newbury D, Joy D, Lyman C, Echlin P, Lifshin E, Sawyer L, Michael J. Scanning electron microscopy and X-ray microanalysis, 3 (Springer, New York, USA), Ch. 5; 2003.

[32] Moncrieff DA, Robinson VNE, Harris LB. Charge neutralisation of insulating surfaces in the SEM by gas ionization. J. Phys. D: Appl. Phys. 1978; 11: 2315.

[33] Toth M, Thiel BL, Donald AM. Interpretation of secondary electron images obtained using a low vacuum SEM. Ultramicroscopy 2003; 94: 71.

[34] Mohan A, Khanna N, Hwu J, Joy DC. Secondary electron imaging in the variable pressure scanning electron microscope. Scanning 1998; 20: 436.

[35] National Institute of Standards and Technology. NIST: Electron-impact cross sections for ionization and excitation. http://physics.nist.gov/PhysRefData/Ionization/ref.html (accessed 12 January 2015).

[36] Haggenmueller R, Gommans HH, Rinzler AG, Fischer JE, Winey KI. Aligned single-wall carbon nanotubes in composites by melt processing methods. Chem. Phys. Lett. 2000; 330: 219.

[37] Zhang X, Liu T, Sreekumar TV, Kumar S, Moore VC, Hauge RH, Smalley RE. Poly(vinyl alcohol)/SWNT composite film. Nano Lett. 2003; 3: 1285.

[38] Shaffer MSP, Windle AH. Fabrication and characterization of carbon nanotube/poly(vinyl alcohol) composites. Adv. Mater. 1999; 11: 937.

[39] Ajayan PM, Stephan O, Colliex C, Trauth D. Aligned carbon nanotubes arrays formed by cutting a polymer resin-nanotube composite. Science 1994; 265: 1212.

[40] Wagner HD, Lourie O, Feldman Y, Tenne R. Stress-induced fragmentation of multi-wall carbon nanotubes in a polymer matrix. Appl. Phys. Lett. 1998; 72 : 188.

[41] Chen Y, Malkovskiy A, Wang XQ, Lebrón-Colón M, Sokolov AP, Perry K, More K, Pang Y. Selection of single-walled carbon nanotube with narrow diameter distribution by using a PPE–PPV copolymer. ACS Macro Letters 2012; 1: 246.

[42] Solá F, Lebrón-Colón M, Ferreira F, Fonseca LF, Meador MA, Marín CJ. In-situ TEM-STM observations of SWCNT ropes/tubular transformations. MRS Proceedings 2009; 1204: 1204-K10-26.

[43] Qin LC. Determination of the chiral indices of carbon nanotubes by electron diffraction. Phys. Chem. Chem. Phys. 2007; 9, 31.

[44] Geim AK, Novoselov KS. The rise of graphene. Nat. Mater. 2007; 6: 183.

[45] Liang Y, Wang H, Sanchez-Casalongue H, Chen Z, Dai H. TiO_2 nanocrystals grown on graphene as advanced photocatalytic hybrid materials. Nano Res. 2010; 3: 701.

[46] Wang B, Wu XL, Shu CY, Guo YG, Wang CR. Synthesis of CuO/graphene nanocomposite as a high-performance anode material for lithium-ion batteries. J. Mater. Chem. 2010; 20: 10661.

[47] Torrisi F, Hasan T, Wu W, Sun Z, Lombardo A, Kulmala TS, Hsieh GW, Jung S, Bonaccorso F, Paul PJ, Chu D and Ferrari AC. Inkjet-printed graphene electronics 2012 ACS Nano 2012; 6: 2992.

[48] Hupalo M, Liu X, Wang C Z, Lu W C, Yao Y X, Ho K M and Tringides M C. Metal Nanostructure formation on Graphene: weak versus strong bonding. Adv. Mater. 2011; 23: 2082.

[49] Xia Y, Xiong Y, Lim B, Skrabalak SE. Shape-controlled synthesis of metal nanocrystals: simple chemistry meets complex physics?. Angew. Chem. Int. Ed. 2009; 48: 60.

[50] Cheng G, Hight Walker AR. Transmission electron microscopy characterization of colloidal copper nanoparticles and their chemical reactivity. Anal. Bioanal. Chem. 2010; 396: 1057.

[51] Kanda KK, Sahu SN, Behera SN. Liquid-drop model for the size-dependent melting of low-dimensional systems. Phys. Rev. A 2002; 66: 013208.

[52] José-Yacamán M, Gutierrez-Wing C, Miki M, Yang DD, Piyakis KN, Sacher E. Surface diffusion and coalescence of mobile metal nanoparticles. J. Phys. Chem. B 2005; 109: 9703.

[53] Tatchev D, Hoell A, Eichelbaum M, Rademann K. X-ray-assisted formation of gold nanoparticles in soda lime silicate glass: suppressed ostwald ripening. Phys. Rev. Lett. 2011; 106: 085702.

[54] Hawa T, Zachariah MR. Coalescence kinetics of unequal sized nanoparticles. J. Aerosol Sci. 2006; 37: 1.

[55] Tao AR, Habas S, Yang P. Shape control of colloidal metal nanocrystals. Small 2008; 4: 310.

[56] Lim TH, McCarthy D, Hendy SC, Stevens KJ, Brown SA, Tilley RD. Real-time TEM and kinetic monte carlo studies of the coalescence of decahedral gold nanoparticles. 2009 ACS Nano; 3: 3809.

[57] Khomyakov PA, Giovannetti G, Rusu PC, Brocks G, van den Brink J, Kelly PJ. First-principles study of the interaction and charge transfer between graphene and metals. Phys. Rev. B 2009; 79: 195425.

[58] Chatterjee B. Anisotropy of melting for cubic metals. Nature 1978; 275: 203.

[59] Shen G, Chen PC, Ryu K, Zhou C. Devices and chemical sensing applications of metal oxide nanowires. J. Mater. Chem. 2009; 19: 828.

[60] Gurlo A. Nanosensors: towards morphological control of gas sensing activity. SnO_2, In_2O_3, ZnO and WO_3 case studies. Nanoscale 2011; 3: 154.

[61] Hunter GW, Dweik RA. Applied breath analysis: an overview of the challenges and opportunities in developing and testing sensor technology for human health monitoring in aerospace and clinical applications. J. Breath Reas. 2008; 2: 037020.

[62] Choi YJ, Hwang IS, Park JG, Chpi KJ, Park JH, Lee JH. Novel fabrication of an SnO(2) nanowire gas sensor with high sensitivity. Nanotechnology 2008; 19: 095508.

[63] Batzill M, Diebold U. The surface and materials science of tin oxide. Prog. Surf. Sci. 2005; 79: 47.

[64] Tiemann M. Porous metal oxides as gas sensors. Chem. – Eur. J 2007; 13: 8376.

[65] Xia Y, Yang P, Sun Y, Wu Y, Mayers B, Gates B, Yin Y, Kim F, Yan H. One-dimensional nanostructures: synthesis, characterization, and applications. Adv. Mater. 2003; 15: 353.

[66] Choi KJ, Jang HW. One-dimensional oxide nanostructures as gas-sensing materials: review and issues. Sensors 2010; 10: 4083.

[67] Lu Y, Li J, Han J, Ng H T, Binder C, Partridge C and Meyyappan M. Room temperature methane detection using palladium loaded single-walled carbon nanotube sensors. Chem. Phys. Lett. 2004; 391: 344.

[68] Li Y, Wang H, Chen Y, Yang M. A multi-walled carbon nanotube/palladium nanocomposite prepared by a facile method for the detection of methane at room temperature. Sens.Act. B 2008; 132: 155.

[69] Lein G, Paquette S, Vadhavkar S, Fuller L, Santhanam KSV. Batron P-Si microsensor for methane and its derivatives. Sens. Act. B 2009; 142: 147.

[70] Moreno MS, Egerton RF, Midgley PA. Electronic structure of tin oxides by electron energy loss spectroscopy and real-space multiple scattering calculations. Phys. Rev. B 2005; 71: 035103.

[71] Kurata H, Lefêvre E, Colliex C, Brydson R. Electron-energy-loss near-edge structures in the oxygen *K*-edge spectra of transition-metal oxides. Phys. Rev. B 1993; 47: 13763.

[72] González GB. Investigating the defect structures in transparent conducting oxides using X-ray and neutron scattering techniques. Materials 2012; 5 : 818.

[73] Filleter T, Espinosa HD. Multi-scale mechanical improvement produced in carbon nanotube fibers by irradiation cross-linking. Carbon 2013; 56: 1-11.

[74] Miller SG, Williams TS, Baker JS, F Solá F, Lebron-Colon M, McCorkle LS, Wilmoth NG, Gaier J, Chen M, Meador MA. Increased tensile strength of carbon nanotube yarns and sheets through chemical modification and electron beam irradiation. ACS applied materials & interfaces 2014; 6: 6120.

[75] Kis A, Csányi G, Salvetat JP, Lee TN, Couteau E, Kulik AJ, Benoit W, Brugger, Forró L. Reinforcement of single-walled carbon nanotube bundles by intertube bridging. Nat Materials 2004; 3: 153 – 157.

[76] Xia ZH, Guduru P, Curtin WA. Enhancing mechanical properties of multi-wall carbon nanotubes via sp^3 inter-wall bridging. Phys Rev Lett 2007; 98: 245501.

[77] Krasheninnikov AV, Nordlund K. Ion and electron irradiation-induced effects in nanostructured materials. J Appl Phys 2010; 107: 071301.

[78] Mikó C, Milas M, Seo JW, Couteau E, Barišić N, Gaál R, Forró L. Effect of electron irradiation on the electrical properties of fibers of aligned single-walled carbon nanotubes. Appl Phys Lett 2003; 83: 4622-4624.

[79] Mikó C, Seo JW, Gaál R, Kulik A, Forró L. Effect of electron and ultraviolet irradiation on aligned carbon nanotube fibers. Phys Status Solidi b 2006; 243: 3351-3354.

[80] Miao M. Electrical conductivity of pure carbon nanotube yarns. Carbon 2011; 49: 3755-3761.

[81] Lambin Ph, Loiseau A, Culot C, Biró LP. Structure of carbon nanotubes probed by local and global probes. Carbon 2002; 40: 1635-1648.

[82] Solá F, Biaggi-Labiosa A, Fonseca LF, Resto O, Lebrón-Colón M, Meador MA. Field emission and radial distribution function studies of fractal-like amorphous carbon nanotips. Nanoscale Res Lett 2009; 4: 431-436.

[83] Solá F, Resto O, Biaggi-Labiosa A, Fonseca LF. Growth and characterization of branched carbon nanostructures arrays in nano-patterned surfaces from porous silicon substrates. Micron 2009; 40, 80-84.

[84] Li L, Solá F, Xia ZH, Yang YQ. Effect of amorphous carbon coatings on the mechanical behavior of silicon carbide nanowire. Journal of Applied Physics 2012; 111, 094306.

[85] St Dennis JE, Venkataraman P, He J, John VT, Obrey SJ, Currier RP, Lebrón-Colón M, Solá F, Meador MA. Rod-like carbon nanostructures produced by the direct pyrolysis of α-cyclodextrin. Carbon 2011; 49: 718-722.

[86] Fonseca LF, Resto O, Solá F. Branched nanostructures and method of synthesizing the same. US Patent 7, 528, 060; 2009.

[87] Solá F, Resto O, Biaggi-Labiosa A, Fonseca LF. Growth of branched carbon nanostructures in nanopatterned surfaces created by focused ion beam. MRS Proceedings 2007; 1059: 1059-KK04-12.

[88] Telling RH, Ewels CP, El-Barbary AA, Heggie MI. Wigner defects bridge the graphite gap. Nat Materials 2003; 2: 333 – 337.

http://dx.doi.org/10.5772/60532

[89] Kruzic JJ, Kimb DK, Koester KJ, Ritchie RO. Indentation techniques for evaluating the fracture toughness of biomaterials and hard tissues. Journal of the mechanical behavior of biomedical materials 2009; 2: 384-395.

[90] Frutos E, González-Carrasco JL. A method to assess the fracture toughness of intermetallic coatings by ultramicroindentation techniques: applicability to coated medical stainless steel. Acta Mater 2013; 61: 1886.

[91] Mingo N, Hauser D, Kobayashi NP, Plissonnier M, Shakouri A. "Nanoparticle-in-alloy" approach to efficient thermoelectrics: silicides in SiGe. Nano Lett 2009; 9:711.

IntechOpen